A generalized circuit model for coupled plasmonic systems

Felix Benz[1], Bart de Nijs[1], Christos Tserkezis[2], Rohit Chikkaraddy[1], Daniel O. Sigle[1], Laurynas Pukenas[3], Stephen D. Evans[3], Javier Aizpurua[2], Jeremy J. Baumberg[1,*]

[1]NanoPhotonics Centre, Cavendish Laboratory, JJ Thompson Ave, University of Cambridge, Cambridge, CB3 0HE, UK

[2]Donostia International Physics Center (DIPC) and Centro de Física de Materiales, Centro Mixto CSIC-UPV/EHU, Paseo Manuel Lardizabal 4, 20018 Donostia/San Sebastián, Spain

[3]Molecular and Nanoscale Physics, School of Physics and Astronomy, University of Leeds, Leeds, LS2 9JT, UK

*Correspondence and requests for materials should be addressed to jjb12@cam.ac.uk

We develop an analytic circuit model for coupled plasmonic dimers separated by small gaps that provides a complete account of the optical resonance wavelength. Using a suitable equivalent circuit, it shows how partially conducting links can be treated and provides quantitative agreement with both experiment and full electromagnetic simulations. The model highlights how, in the conducting regime, the kinetic inductance of the linkers set the spectral blue-shifts of the coupled plasmon.

Keywords: circuit model, plasmonics, nanophotonics, plasmonic coupling, quantum plasmonics, conductivity.

Plasmonic nanostructures are at the heart of many research fields ranging from biological applications[1,2] to quantum information processing[3,4]. In recent years significant progress has been made in both the chemical preparation of noble-metal nanostructures[5] and in simulation tools to model them[6–10]. However few attempts have been made to develop a comprehensive analytical model [11,12] that could facilitate direct validation of experimental results and yield parameters that can guide the implementation of full electromagnetic simulations. Most analytical approaches approximate Maxwell's equations and are limited to specific geometries. A promising alternative is to treat any nanoplasmonic system as a high frequency circuit composed of capacitors, inductors, and resistors [13–15]. Such a circuit model is extremely versatile as generalized equations for the resonance condition can be obtained, and their dependence on the geometry of the nanostructure understood explicitly. Here we use this circuit approach to develop a simple analytical expression for two coupled plasmonic systems in close proximity. Surprisingly this has been absent until now, despite its extreme utility, because a number of subtle effects need to be considered. Our model is

capable of describing both insulating and conductive gaps and applicable to arbitrary coupled plasmonic systems.

We start from the description of a single spherical nanoparticle, which is well characterized by an LC circuit. Engetha *et al.* [6] have determined the impedance contributions of the fringing field $Z_{\text{fringe}}^{-1} = -i\omega C_s = -i2\pi\omega R \varepsilon_0$ and the sphere $Z_{\text{sphere}}^{-1} = -i\pi\omega R \varepsilon \varepsilon_0$ with nanoparticle radius R, frequency ω, nanoparticle dielectric function, with gold permittivity ε, vacuum permittivity ε_0, and the capacitance due to the fringing field C_s. For a metallic nanoparticle ε is negative and therefore the impedance contribution of the sphere is inductive. The resonance wavelength can be determined by $\Im m(1/Z_{tot}) = 0$, which yields the well-known resonance condition in the electrostatic case for a plasmonic nanoparticle $\varepsilon = -2$. Here, throughout we use a Drude model for the dielectric function of gold:

$$\varepsilon = \varepsilon_\infty - \left(\frac{\omega_p}{\omega}\right)^2 = \varepsilon_\infty - \left(\frac{\lambda}{\lambda_p}\right)^2 \tag{1}$$

This yields the single particle resonance frequency, $\lambda_s^2 = \lambda_p^2 (\varepsilon_\infty + 2)$. The plasma frequency and wavelength (ω_p and λ_p respectively), and the background high frequency permittivity (ε_∞) are material parameters which should not depend on nanoparticle size. However, electrodynamical effects, beyond the electrostatic approximation, lead to a weak particle size dependence of the resonance wavelength. There are several ways of correcting the resonance condition due to retardation [16,17], however, a relatively simple phenomenological way to account for this is to assume that ε_∞ depends slightly on the nanoparticle size. The resonance wavelength of different gold nanoparticle sizes in water (permittivity ε_m=1.33) from extinction spectroscopy (Fig.1) provides estimated values for $\varepsilon_\infty(R)$ using $\varepsilon = -2\varepsilon_m$ together with Eq.(1).
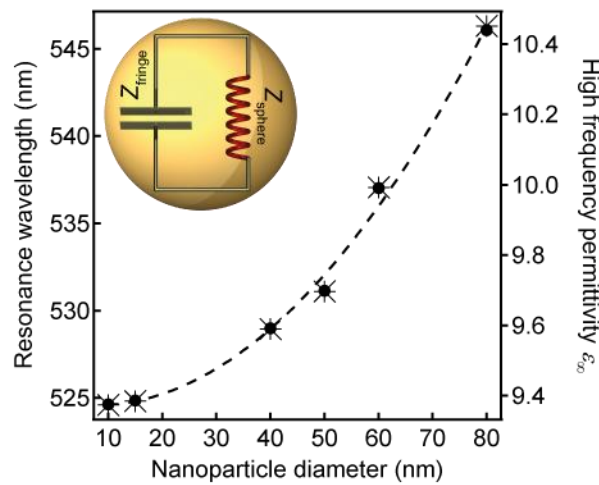
Figure 1. Resonance wavelength for different nanoparticle sizes and resulting values for ε_∞. Inset: Single

nanoparticle equivalent LC-circuit.

To describe purely capacitive-coupled resonances a capacitor (with capacitance C_g) can be placed between two equivalent single particle circuits mimicking the capacitive coupling, which reproduces the strongly red-shifted resonance[18,19]. However, for either a conductive spacer[20] or for very small gaps[21,22] effects due to the increasing conductivity between the two systems have to be considered, with two results: First, the coupled bonding dimer plasmon mode (BDP) blue-shifts due to screening of the local field in the gap, forming the screened coupled mode (SBDP). In this conductivity region the screening field reduces the voltage between the two elements. Second, for higher conductivities a charge transfer mode, characterized by a net current between the two nanoparticles is formed[23]. Since both modes have different physical origins they have to be described by different equivalent circuits. Here we restrict ourselves to the screening of the coupled mode as this is directly accessible in our optical experiments.
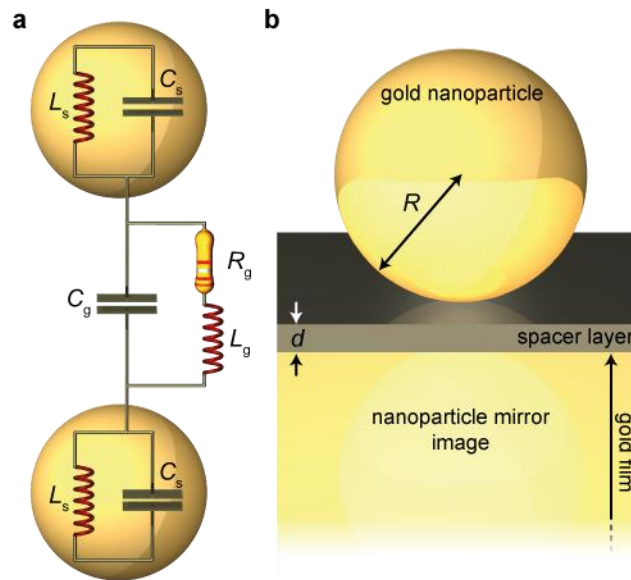
Figure 2. Illustration of the used circuit model and the nanoparticle on mirror geometry. **a** Equivalent circuit for a coupled plasmon mode with both purely capacitive coupling and conductive coupling. **b** Illustration of the nanoparticle on mirror (NPoM) geometry.

Previously we considered the ratio of the screened charge to the charge stored on a capacitor without any conductive link[20]. This simplified picture can be described by a resistor in series with the coupling capacitor effectively reducing the voltage at the capacitor. While this approach works well for describing relative changes of the charge stored on the capacitor per optical cycle it is not capable of predicting the absolute value of the resonance wavelength. Therefore we use here an equivalent parallel circuit, which

is composed of a capacitor shunted with a resistor and an inductor, which reproduces the behaviour of conductive paths through the gap, in series (see Fig.2a). For a sufficiently low resistance the inductor produces a screening voltage, while for high resistance the inductor plays no role and the coupling is purely dominated by the capacitor. If the gap inductance is large, then little screening is obtained because charge cannot short across the gap within an optical cycle. Hence the fully screened mode at large conductance is blue-shifted furthest if the gap inductance approaches the inductance given by the individual sphere.

The resonance frequency of this circuit found when $\Im m(1/Z_{tot}) = 0$ is

$$Z_{tot} = \frac{2}{-2i\pi\omega R\varepsilon_m\varepsilon_0 - i\pi\omega R\varepsilon\varepsilon_0} + \frac{1}{-i\omega C_g + [R - i\omega L_g]^{-1}} \tag{2}$$

Simplifying this equation (see supplementary material) yields the resonance condition:

$$\widetilde{\omega}^4 + \widetilde{\omega}^2 \left[\omega_d^2 \left(\frac{4\varepsilon_m}{\Gamma} - 1\right) + \delta\right] - \omega_d^2\delta = 0 \tag{3}$$

where $\widetilde{\omega} = \omega/\omega_p$ is the normalised resonance frequency, the dimer mode $\omega_d = 1/\sqrt{2\varepsilon_m + \varepsilon_\infty + 4\varepsilon_m\eta}$, normalised gap capacitance $\eta = C_g/C_s$, normalised inductive coupling rate $\Gamma = -L_g C_s \omega_p^2$, and normalised loss rate $\delta = \left(\frac{R_g}{L_g\omega_p}\right)^2$. For the case of very low conductivity ($R_g \to 0$) which gives the typical coupled mode of the bonding dimer plasmon (BDP) this can be simplified to $\widetilde{\omega} = \omega_d$ giving resonant wavelength

$$\lambda_d = \lambda_p\sqrt{2\varepsilon_m + \varepsilon_\infty + 4\varepsilon_m\eta} \tag{4}$$

for coupled plasmonic particles. In the extreme case of high conductivity ($R_g \to \infty$ so $\delta^{-1} \to 0$), eq.(3) yields the screened coupled plasmon mode (SBDP)

$$\lambda_{SBDP} = \lambda_d / \sqrt{1 - \frac{4\varepsilon_m}{\Gamma}} \tag{5}$$

which is a central result of our paper.

We now use the nanoparticle on mirror geometry to test this model. In this geometry a gold nanoparticle is placed on a thin spacer layer above a gold film (Fig.2b). Dipoles induced in the nanoparticle can couple to their image charges forming a tightly confined coupled plasmon mode[24]. The gap capacitance for this geometry can be obtained following Hudlet *et al.*[25] (see Supplementary Material):

$$C_g = 2\pi\varepsilon_0 (n_g)^\chi R . \ln\left[1 + \frac{R}{2d}\theta_{max}^2\right] \tag{6}$$

with refractive index of the material in the gap n_g, separation between nanoparticle and gold film d, and parameters θ_{max} (which arises from the laterally localised electric field) and χ=1.14 (which arises

from the specific NPoM geometry, Suppl. Info. S2). To check the validity of the model simulations were performed using the full electrodynamic boundary-element method (BEM)[6,26].
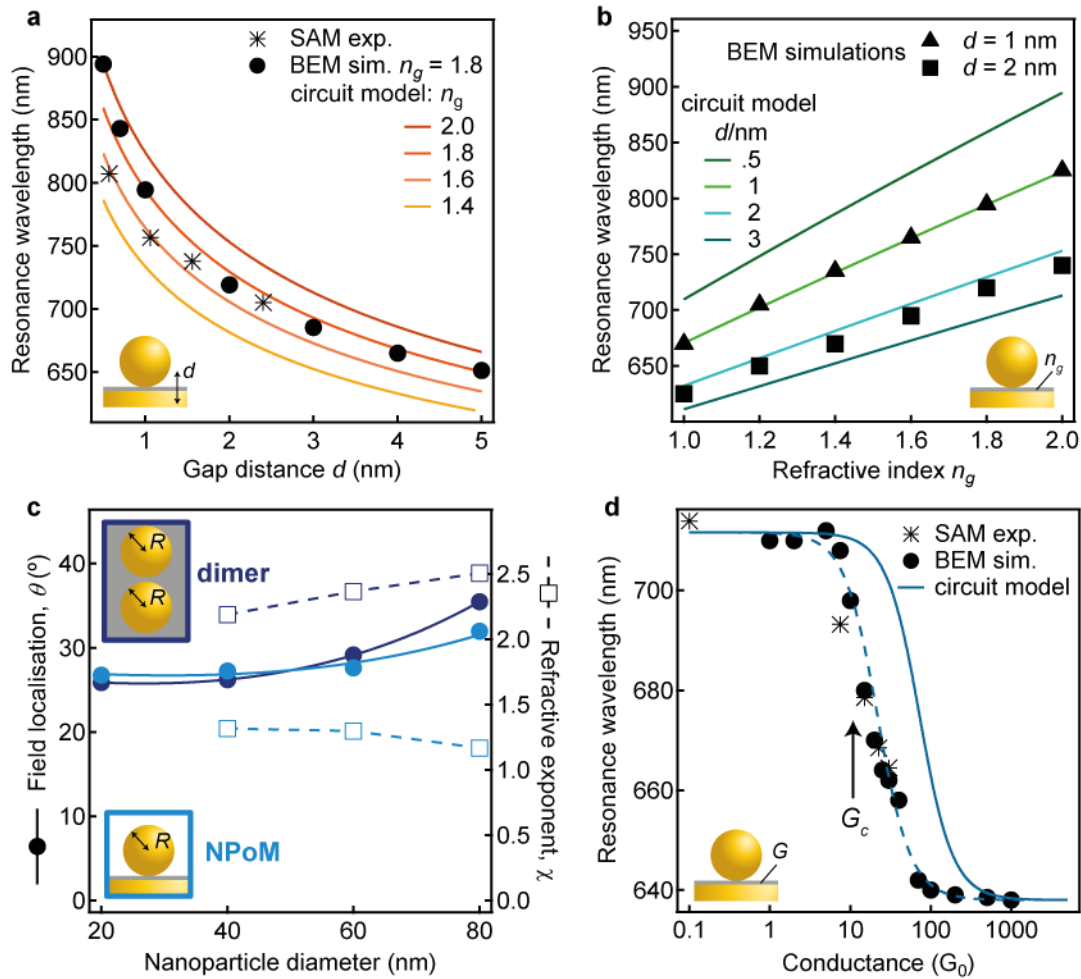

Figure 3. Comparison of the presented circuit model to experimental and simulated data. **a,b** Coupled plasmon mode with R=40nm NPoM for different gap separations and refractive indices. **c** Nanoparticle size and geometry dependence of the lateral field localisation (solid circles, expressed in terms of the angle θ_{max}, see supp. info.) and refractive index exponent, χ (empty squares). **d** Blue-shift of the coupled plasmon mode as gap conductance increases, for R=30nm, simulated and experimental data from[20]. The dashed line is shifted by 170G_0- (see main text).

Additional experimental data are obtained by assembling spacers of self-assembled monolayers (SAMs) of aliphatic monothiols CH_3-$(CH_2)_x$-SH with x from 3 to 17. The thickness of each SAM is measured using a spectroscopic ellipsometry. Subsequently, 80 nm gold nanoparticles are assembled on top of these SAMs. The resonance wavelengths in air (ε_m=1) of more than 1,000 particles per sample were recorded using a fully automated darkfield microscope and cooled spectrometer. The average resonance wavelengths and standard errors were determined by fitting Gaussian distributions to the histograms (see supplementary material).

Comparing our analytical circuit model, BEM simulations, and experimental data shows excellent agreement. The characteristic continuous blueshift of the coupled plasmon resonance for increasing gap spacing and different refractive indices is clearly shown in Fig.3(a). Similarly the expected linear redshift with increasing refractive index is completely reproduced (Fig.3b).

The gap capacitance parameters are found to be weakly dependent on the nanoparticle size and geometry (Fig.3c). This is because the field localisation (described here by θ_{max}) is slightly different between NPoM and two nanoparticles in a dimer, in particular in the effects of increasing the spacer refractive index (see Supp. Info. S2). Most crucially, the model predicts for the first time analytically the blue shift of the coupled plasmon when the gap starts conducting (Fig.3d). While such effects from mixed conducting SAM layers have only previously been computed in full simulations[23], our analytic solution indeed captures three important properties of such a conductive system: (i) the need to exceed a critical conductance G_c, (ii) continuous blue shifts with increasing conductance, and (iii) the saturation of the screening for large conductances. The exact critical conductance is overestimated in our model (Fig.3d solid line), and fits much better when shifted by -170G_0 (dashed Fig.3d), however the order of magnitude is acceptable. Using eqn.(3), we obtain an analytical estimate for the critical conductance, $\frac{G_c}{G_0} \simeq \frac{4\pi^2}{G_0 Z_0} \frac{R}{\lambda_p} \frac{\lambda_d}{\Gamma}$ where Z_0=377Ω is the impedance of free space (see Supp.Info.).
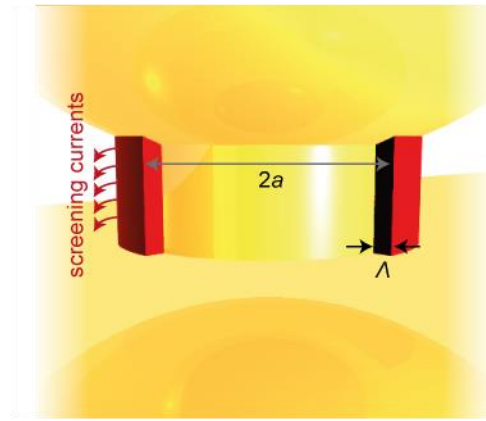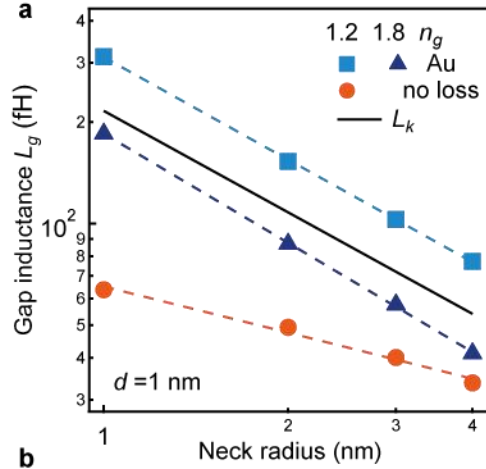
Figure 4. Interpretation of the introduced gap inductance. **a** Gap inductance *vs* neck radius, extracted by using Eqn.(5) on simulation results, and compared to kinetic inductance model (solid line). Filaments are either gold, or near-perfect conductor. **b** Schematic of sheath currents confined to penetration depth Λ down conducting filament, which gives kinetic inductance.

The maximum blue shift when the gap becomes conducting (saturating the screening) is set by the inductance of this filament, which screens charges in the gap expelling the electric field. To understand what sets the value of this inductance we perform BEM simulations for both insulating and completely conducting gaps. The conductive region was modelled as a cylinder connecting the gold spheres. Varying the neck radius a reveals that $L_g \propto a^{-1}$ for gold while for an ideal conductor (with extremely low damping) we find $L_g \propto a^{-0.5}$ (Fig.4a). This dependence arises because L_g is dominated by the kinetic inductance L_k produced by the magnetic field in the gap encircling the current acting to drag back the electrons. To get L_k we equate the kinetic energy of N moving electrons with the energy of an inductor $N\frac{1}{2}mv^2 = \frac{1}{2}L_k I^2$ with velocity v, current $I = nevA$, area A, and $N = nAd$, giving $L_k = \frac{d}{A}\frac{m}{ne^2} = \frac{d}{A\varepsilon_0\omega_p^2}$ with density of mobile carriers in the conducting link n and electron mass m^{27}. The electric field however can

only penetrate a certain distance Λ into the connecting filament so that current flows only in an outer sheath (Fig.4b) giving

$$L_k = \frac{1}{\varepsilon_0 \omega_p^2} \frac{d+2\Lambda}{2\pi\Lambda a} = \frac{1}{\varepsilon_0 \omega_p^2} \frac{f}{a} \tag{7}$$

with the geometry factor $f = \frac{1}{\pi}[1 + d/2\Lambda]$. We find screening depths of $\Lambda \sim$ 3nm (Supp.Info.) so for very narrow gold gaps, $f \rightarrow 1/\pi$ which then accounts extremely well for the a^{-1} dependence in the full simulations of L_g and even produces *quantitative* agreement with the magnitude of the gap inductance (Fig.4a). For an imperfect metal the screening depth cannot be ignored, giving a modified form which depends also on n_g (Supp.Info.). The blue-shift of the coupled plasmon seen when conducting links are inserted between plasmonic elements can thus be understood as arising from their kinetic inductance. Inserting Eqn.(7) into Eqn.(5), we find an analytic form of the blue-shift

$$\frac{\Delta\lambda}{\lambda} = \varepsilon_m \frac{a}{R} \left(1 + \frac{d}{2\Lambda}\right)^{-1} \tag{8}$$

which for small gaps depends linearly on the ratio of neck to nanoparticle radius. These shifts can indeed be large (we obtain 70nm spectral shifts experimentally, see Fig.3d). We also note the interesting ramification that $\Delta\lambda$ will depend on the morphology of links across a plasmonic gap. This opens great opportunities in understanding nanoscale conducting elements purely through optical spectroscopy, which can then follow dynamic processes.

In conclusion, we present a circuit model which can be used to describe coupled plasmon resonances in both capacitive and conductive coupling regimes. It provides an exceptionally straightforward way to calculate analytically the resonance wavelength for different gap sizes, nanoparticle sizes, refractive indices, and linker conductivities. We showed how a test geometry based on a nanoparticle on gold mirror gives excellent agreement of the model with both experiment and simulation. This model allows us to identify the crucial properties of the system, and resolves the key role of kinetic inductance. Further geometries can easily be incorporated by adjusting the capacitances of both the gap region and the individual plasmonic systems.

Methods

Sample Preparation

A 100 nm thick gold film was evaporated on a silicon (100) wafer (Kurt J. Lesker Company, PVD 200) using an evaporation rate of 1 Å/s with a base pressure of ≈1 × 10^{-7} mbar. To obtain atomically smooth

gold surfaces a standard template stripping method was applied: small silicon (100) pieces were glued to the evaporated gold surface using Epo-Tek 377 epoxy glue. After curing the glue the sample can be pealed of the silicon wafer revealing a fresh, clean surface with excellent surface roughness[28]. 1-butanethiol (C_4), 1-pentanethiol (C_5), 1-nonanethiol (C_9), 1-dodecanethiol (C_{12}), and 1-octadecanethiol (C_{18}) (Sigma-Aldrich, ≥98%) self-assembled monolayers were assembled on these freshly prepared surfaces by immersing in 1 mM solution for ≈22 h. Subsequently, the samples were thoroughly rinsed with ethanol, briefly cleaned in an ultrasonic bath to remove excess unbound thiols, and blown dry. The samples were stored under a constant nitrogen flow until they were used. 80 nm gold nanoparticles were used as received from BBI Solutions. To deposit the nanoparticles on the SAM the previously prepared samples were immersed in the nanoparticle solution. The time was adjusted in order to reach a uniform but sparse coverage that allows spectroscopic investigations of individual nanoparticles. Excess nanoparticles were rinsed off with distilled water and the samples were dried with nitrogen.

Experimental

Darkfield spectra of over 1,000 nanoparticles were recorded using a fully automated Olympus BX51 microscope in a reflective dark field geometry. The scattered light was collected with a ×100 long working distance objective (NA 0.75) and analysed with a TEC-cooled Ocean Optics QE65000 spectrometer. Further details can be found elsewhere[29].

Ellipsometry

The thickness of the self-assembled monolayers was measured using a Jobin-Yvon UVISEL spectroscopic ellipsometer at angle of incidence 70° and wavelengths from 300-800 nm. The base layer permittivity is obtained from a clean gold substrate and the dielectric properties of the SAMs described using a Cauchy model with refractive index of 1.45 (as determined by[30,31]).

Simulations

Far-field extinction spectra are calculated by numerical simulations using the full electrodynamic boundary-element method (BEM)[6,26]. The BEM method solves Maxwell's equations for inhomogeneous media characterised by local dielectric functions in terms of surface-integral equations of the induced charges and currents, which are obtained through discretisation of the surface integrals and solution of the resulting matrix equations. The EM field is then calculated in terms of these induced charges and currents. A sufficient number of discretisation points were used to ensure full convergence of all results.

Acknowledgements

Author contributions

The model was developed by FB and JJB. Experiments were planned and executed by FB, BdN, LP, SDE, and JJB. Simulations were performed by CT, RC, DOS and JA. The data was analysed by FB and JJB and all authors contributed to the manuscript.

Additional information

The authors declare no competing financial interests.

Supporting Information Available: Derivation of the model, additional information on the capacitance model, additional experimental data. This material is available free of charge via the Internet at http://pubs.acs.org.

References

(1)   Homola, J. *Chem. Rev.* **2008**, *108* (2), 462–493.
(2)   Taylor, R. W.; Benz, F.; Sigle, D. O.; Bowman, R. W.; Bao, P.; Roth, J.; Heath, G. R.; Evans, S. D.; Baumberg, J. J. *Sci. Rep.* **2014**, *4*, 5940.
(3)   Di Martino, G.; Sonnefraud, Y.; Tame, M. S.; Kéna-Cohen, S.; Dieleman, F.; Özdemir, Ş. K.; Kim, M. S.; Maier, S. A. *Phys. Rev. Appl.* **2014**, *1* (3), 034004.
(4)   Di Martino, G.; Sonnefraud, Y.; Kéna-Cohen, S.; Tame, M.; Özdemir, Ş. K.; Kim, M. S.; Maier, S. A. *Nano Lett.* **2012**, *12* (5), 2504–2508.
(5)   Itoh, H.; Naka, K.; Chujo, Y. *J. Am. Chem. Soc.* **2004**, *126* (10), 3026–3027.
(6)   García de Abajo, F. J.; Aizpurua, J. *Phys. Rev. B* **1997**, *56* (24), 15873–15884.
(7)   Esteban, R.; Borisov, A. G.; Nordlander, P.; Aizpurua, J. *Nat. Commun.* **2012**, *3*, 825.
(8)   Salandrino, A.; Engheta, N. *Phys. Rev. B* **2006**, *74* (7), 075103.
(9)   Pelton, M.; Aizpurua, J.; Bryant, G. *Laser Photonics Rev.* **2008**, *2* (3), 136–159.
(10)   Taflove, A.; Hagness, Susan C. *Computational Electrodynamics: The Finite-Difference Time-Domain Method*, 3. ed.; Artech House: Boston, 2005.
(11)   Dhawan, A.; Norton, S. J.; Gerhold, M. D.; Vo-Dinh, T. *Opt. Express* **2009**, *17* (12), 9688–9703.
(12)   Trivedi, R.; Thomas, A.; Dhawan, A. *Opt. Express* **2014**, *22* (17), 19970.
(13)   Engheta, N.; Salandrino, A.; Alù, A. *Phys. Rev. Lett.* **2005**, *95* (9), 095504.
(14)   Engheta, N. *Science* **2007**, *317* (5845), 1698–1702.

(15)   Liu, N.; Wen, F.; Zhao, Y.; Wang, Y.; Nordlander, P.; Halas, N. J.; Alù, A. *Nano Lett.* **2013**, *13* (1), 142–147.

(16)   Myroshnychenko, V.; Rodríguez-Fernández, J.; Pastoriza-Santos, I.; Funston, A. M.; Novo, C.; Mulvaney, P.; Liz-Marzán, L. M.; Abajo, F. J. G. de. *Chem. Soc. Rev.* **2008**, *37* (9), 1792–1805.

(17)   Sarychev, A. K.; Shalaev, V. M. *Phys. Rep.* **2000**, *335* (6), 275–371.

(18)   Jain, P. K.; Huang, W.; El-Sayed, M. A. *Nano Lett.* **2007**, *7* (7), 2080–2088.

(19)   Sönnichsen, C.; Reinhard, B. M.; Liphardt, J.; Alivisatos, A. P. *Nat. Biotechnol.* **2005**, *23* (6), 741–745.

(20)   Benz, F.; Tserkezis, C.; Herrmann, L. O.; de Nijs, B.; Sanders, A.; Sigle, D. O.; Pukenas, L.; Evans, S. D.; Aizpurua, J.; Baumberg, J. J. *Nano Lett.* **2015**, *15* (1), 669–674.

(21)   Savage, K. J.; Hawkeye, M. M.; Esteban, R.; Borisov, A. G.; Aizpurua, J.; Baumberg, J. J. *Nature* **2012**, *491* (7425), 574–577.

(22)   Scholl, J. A.; García-Etxarri, A.; Koh, A. L.; Dionne, J. A. *Nano Lett.* **2013**, *13* (2), 564–569.

(23)   Pérez-González, O.; Zabala, N.; Borisov, A. G.; Halas, N. J.; Nordlander, P.; Aizpurua, J. *Nano Lett.* **2010**, *10* (8), 3090–3095.

(24)   Nordlander, P.; Prodan, E. *Nano Lett.* **2004**, *4* (11), 2209–2213.

(25)   Hudlet, S.; Saint Jean, M.; Guthmann, C.; Berger, J. *Eur. Phys. J. B* **1998**, *2* (1), 5–10.

(26)   García de Abajo, F. J.; Howie, A. *Phys. Rev. B* **2002**, *65* (11), 115418.

(27)   Staffaroni, M.; Conway, J.; Vedantam, S.; Tang, J.; Yablonovitch, E. *Photonics Nanostructures - Fundam. Appl.* **2012**, *10* (1), 166–176.

(28)   Hegner, M.; Wagner, P.; Semenza, G. *Surf. Sci.* **1993**, *291* (1–2), 39–46.

(29)   Nijs, B. de; Bowman, R. W.; Herrmann, L. O.; Benz, F.; Barrow, S. J.; Mertens, J.; Sigle, D. O.; Chikkaraddy, R.; Eiden, A.; Ferrari, A.; Scherman, O. A.; Baumberg, J. J. *Faraday Discuss.* **2015**, *178* (0), 185–193.

(30)   Folkers, J. P.; Laibinis, P. E.; Whitesides, G. M. *Langmuir* **1992**, *8* (5), 1330–1341.

(31)   Bain, C. D.; Troughton, E. B.; Tao, Y. T.; Evall, J.; Whitesides, G. M.; Nuzzo, R. G. *J. Am. Chem. Soc.* **1989**, *111* (1), 321–335.

Table of Contents Graphic